Fast three-dimensional terahertz computed tomography using real-time line projection of intense terahertz pulse

Mukesh Jewariya,[1] Emmanuel Abraham,[2,3] Takayuki Kitaguchi,[1] Yoshiyuki Ohgi,[4] Masa-aki Minami,[4] Tsutomu Araki,[4] and Takeshi Yasui[1,4,*]

[1]*Institute of Technology and Science, University of Tokushima, 2-1, Minami-Josanjima-cho, Tokushima, Tokushima 770-8506, Japan*

[2]*LOMA, University of Bordeaux - CNRS, UMR 5798, 351 Cours de la Libération, 33405 Talence, France*

[3]*em.abraham@loma.u-bordeaux1.fr*

[4]*Graduate School of Engineering Science, Osaka University, 1-3, Machikaneyama-cho, Toyonaka, Osaka 560-8531, Japan*

**yasui.takeshi@tokushima-u.ac.jp*

Abstract: We demonstrated fast three-dimensional transmission terahertz computed tomography by using real-time line projection of intense terahertz beam generated by optical rectification in lithium niobate crystal. After emphasizing the advantage of intense terahertz pulse generation for two-dimensional spatio-temporal terahertz imaging, peak-to-peak amplitudes of pulsed terahertz electric field have been used to obtain a series of projection images at different rotation angles. Then a standard reconstruction algorithm has been employed to perform final three-dimensional reconstruction. Test samples including a medicine capsule have been investigated with a total acquisition time to only 6 minutes.

OCIS codes: (110.6795) Terahertz imaging; (110.6955) Tomographic imaging; (100.6890) Three-dimensional image processing; (320.7090) Ultrafast lasers.

References and links

1. G. T. Herman, Image *Reconstruction from Projections: The Fundamentals of Computerized Tomography* (Academic, 1980).
2. M. J. Aitken, *Thermoluminescence Dating* (Academic, 1985).
3. W. L. Chan, J. Deibel, and D. M. Mittleman, "Imaging with terahertz radiation," Rep. Prog. Phys. **70**(8), 1325–1379 (2007).
4. B. Ferguson, S. Wang, D. Gray, D. Abbot, and X.-C. Zhang, "T-ray computed tomography," Opt. Lett. **27**(15), 1312–1314 (2002).
5. X. Yin, B. W. H. Ng, and D. Abbott, *Terahertz Imaging for Biomedical Applications: Pattern Recognition and Tomographic Reconstruction* (Springer, 2012).
6. A. Brahm, M. Kunz, S. Riehemann, G. Notni, and A. Tünnermann, "Volumetric spectral analysis of materials using terahertz-tomography techniques," Appl. Phys. B **100**(1), 151–158 (2010).
7. E. Abraham, A. Younus, C. Aguerre, P. Desbarats, and P. Mounaix, "Refraction losses in terahertz computed tomography," Opt. Commun. **283**(10), 2050–2055 (2010).
8. K. L. Nguyen, M. L. Johns, L. F. Gladden, C. H. Worrall, P. Alexander, H. E. Beere, M. Pepper, D. A. Ritchie, J. Alton, S. Barbieri, and E. H. Linfield, "Three-dimensional imaging with a terahertz quantum cascade laser," Opt. Express **14**(6), 2123–2129 (2006).
9. J. P. Caumes, A. Younus, S. Salort, B. Chassagne, B. Recur, A. Ziéglé, A. Dautant, and E. Abraham, "Terahertz tomographic imaging of XVIIIth dynasty Egyptian sealed pottery," Appl. Opt. **50**(20), 3604–3608 (2011).
10. M. Bessou, H. Duday, J. P. Caumes, S. Salort, B. Chassagne, A. Dautant, A. Ziéglé, and E. Abraham, "Advantages of terahertz radiation versus X-ray to detect hidden organic materials in sealed vessels," Opt. Commun. **285**(21–22), 4175–4179 (2012).
11. M. Bessou, B. Chassagne, J. P. Caumes, C. Pradère, P. Maire, M. Tondusson, and E. Abraham, "Three-dimensional terahertz computed tomography of human bones," Appl. Opt. **51**(28), 6738–6744 (2012).
12. N. Sunaguchi, Y. Sasaki, N. Maikusa, M. Kawai, T. Yuasa, and C. Otani, "Depth-resolving THz imaging with tomosynthesis," Opt. Express **17**(12), 9558–9570 (2009).
13. T. Yasui, E. Saneyoshi, and T. Araki, "Asynchronous optical sampling terahertz time-domain spectroscopy for ultrahigh spectral resolution and rapid data acquisition," Appl. Phys. Lett. **87**(6), 061101 (2005).
14. Q. Wu, T. D. Hewitt, and X.-C. Zhang, "Two-dimensional electro-optic imaging of THz beams," Appl. Phys. Lett. **69**(8), 1026–1028 (1996).

#182051 - $15.00 USD Received 19 Dec 2012; revised 17 Jan 2013; accepted 17 Jan 2013; published 24 Jan 2013

15. T. Yasuda, T. Yasui, T. Araki, and E. Abraham, "Real-time two-dimensional terahertz tomography of moving objects," Opt. Commun. **267**(1), 128–136 (2006).
16. T. Yasui, K. Sawanaka, A. Ihara, E. Abraham, M. Hashimoto, and T. Araki, "Real-time terahertz color scanner for moving objects," Opt. Express **16**(2), 1208–1221 (2008).
17. M. Schirmer, M. Fujio, M. Minami, J. Miura, T. Araki, and T. Yasui, "Biomedical applications of a real-time terahertz color scanner," Biomed. Opt. Express **1**(2), 354–366 (2010).
18. J. Shan, A. S. Weling, E. Knoesel, L. Bartels, M. Bonn, A. Nahata, G. A. Reider, and T. F. Heinz, "Single-shot measurement of terahertz electromagnetic pulses by use of electro-optic sampling," Opt. Lett. **25**(6), 426–428 (2000).
19. J. Hebling, K.-L. Yeh, M. C. Hoffmann, B. Bartal, and K. A. Nelson, "Generation of high-power terahertz pulses by tilted-pulse-front excitation and their application possibilities," J. Opt. Soc. Am. B **25**(7), B6–B19 (2008).
20. M. Jewariya, M. Nagai, and K. Tanaka, "Enhancement of terahertz wave generation by cascaded $\chi^{(2)}$ processes in $LiNbO_3$," J. Opt. Soc. Am. B **26**(9), A101–A106 (2009).
21. J. A. Fülöp, L. Pálfalvi, G. Almási, and J. Hebling, "Design of high-energy terahertz sources based on optical rectification," Opt. Express **18**(12), 12311–12327 (2010).
22. J. A. Fülöp, L. Pálfalvi, M. C. Hoffmann, and J. Hebling, "Towards generation of mJ-level ultrashort THz pulses by optical rectification," Opt. Express **19**(16), 15090–15097 (2011).
23. H. Hirori, A. Doi, F. Blanchard, and K. Tanaka, "Single-cycle terahertz pulses with amplitudes exceeding 1 MV/cm generated by optical rectification in $LiNbO_3$," Appl. Phys. Lett. **98**(9), 091106 (2011).
24. M. Nagai, E. Matsubara, and M. Ashida, "High-efficiency terahertz pulse generation via optical rectification by suppressing stimulated Raman scattering process," Opt. Express **20**(6), 6509–6514 (2012).
25. M. Jewariya, M. Nagai, and K. Tanaka, "Ladder climbing on the anharmonic intermolecular potential in an amino acid microcrystal via an intense monocycle terahertz pulse," Phys. Rev. Lett. **105**(20), 203003 (2010).
26. K. Tanaka, H. Hirori, and M. Nagai, "THz nonlinear spectroscopy of solids," IEEE Trans. Terahertz Sci. Technol. **1**(1), 301–312 (2011).
27. A. Doi, F. Blanchard, H. Hirori, and K. Tanaka, "Near-field THz imaging of free induction decay from a tyrosine crystal," Opt. Express **18**(17), 18419–18424 (2010).
28. F. Blanchard, A. Doi, T. Tanaka, H. Hirori, H. Tanaka, Y. Kadoya, and K. Tanaka, "Real-time terahertz near-field microscope," Opt. Express **19**(9), 8277–8284 (2011).
29. Z. Jiang, X. G. Xu, and X.-C. Zhang, "Improvement of terahertz imaging with a dynamic subtraction technique," Appl. Opt. **39**(17), 2982–2987 (2000).
30. E. Abraham, Y. Ohgi, M. A. Minami, M. Jewariya, M. Nagai, T. Araki, and T. Yasui, "Real-time line projection for fast terahertz spectral computed tomography," Opt. Lett. **36**(11), 2119–2121 (2011).
31. T. Yasui, M. Jewariya, T. Yasuda, M. Schirmer, T. Araki, and E. Abraham, "Real- time two-dimensional spatio-temporal terahertz imaging based non-collinear free-space electro-optic sampling application to functional terahertz imaging of moving object," IEEE J. Sel. Top. Quantum Electron. **19**(1), (2013), doi:10.1109/JSTQE.2012.2210393.
32. F. Miyamaru, T. Yonera, M. Tani, and M. Hangyo, "Terahertz two-dimensional electrooptic sampling using high speed complementary metal-oxide semiconductor camera," Jpn. J. Appl. Phys. **43**(4A 4A), L489–L491 (2004).
33. W. S. Rasband, ImageJ (U.S. National Institutes of Health, Bethesda, Maryland, USA) *http://imagej.nih.gov/ij/*, 1997–2012.
34. B. Recur, A. Younus, S. Salort, P. Mounaix, B. Chassagne, P. Desbarats, J.-P. Caumes, and E. Abraham, "Investigation on reconstruction methods applied to 3D terahertz computed tomography," Opt. Express **19**(6), 5105–5117 (2011).
35. M. D. Thomson, M. Kreß, T. Löffler, and H. G. Roskos, "Broadband THz emission from gas plasmas induced by femtosecond optical pulses: From fundamentals to applications," Laser & Photon. Rev. **1**(4), 349–368 (2007).
36. T. T. L. Kristensen, W. Withayachumnankul, P. U. Jepsen, and D. Abbott, "Modeling terahertz heating effects on water," Opt. Express **18**(5), 4727–4739 (2010).

1. Introduction

Computed tomography (CT) is an effective imaging method to visualize the internal structure of a three-dimensional (3D) object as cross-sectional images. In this method, a series of transmitted images are measured at different projection angles and the internal structure of the object is reconstructed by analyzing these images with specific reconstruction algorithms, such as the filtered back-projection (FBP) algorithm using Radon inverse transform [1]. Conventionally, X-ray CT has been widely used in non-destructive testing, quality control, material characterization and biomedical imaging [2]. However, the hazardous ionizing effects of X-ray often limit its utility. Also, high penetration power of X-ray reduces image contrast in composite or soft materials, such as plastics or ceramics. Furthermore, this imaging modality only produces monochrome pictures of the sample, making it difficult to identify its chemical components.

Recently, terahertz (THz) radiation has emerged as a new mode for CT because of free-space propagation, low photon energy, moderate penetration through soft materials and broad

#182051 - $15.00 USD Received 19 Dec 2012; revised 17 Jan 2013; accepted 17 Jan 2013; published 24 Jan 2013

spectral range [3]. Since the first demonstration of THz CT in 2002 [4], it has been successively used to visualize internal structures of various objects from industrial, pharmaceutical to biological applications [5-12]. Moreover, THz spectral CT can provide colored pictures in THz range as compared to monochrome X-ray CT, associated to the possibility to tentatively analyze the chemical composition of the sample based on THz spectral fingerprints. However, considering practical applications of THz CT, we have to face a strong limitation which is the long acquisition time arising from use of THz time-domain spectroscopy (THz-TDS). This is because THz-CT based on THz-TDS needs serial scanning of four mechanical stages for time delay, two-dimensional (2D) sample position and sample rotation to record the series of THz projection images at multiple angles. In particular, the mechanical stage for time-delay scanning is the most time-consuming due to its reciprocating motion.

The simplest way to reduce time-delay scanning is to use a fast scanning mechanical delay stage. Asynchronous optical sampling (ASOPS) is another promising method without any mechanical delay [13]. However, to accomplish adequate signal-to-noise ratio and high dynamic range, multiple scans have to be integrated together associated with the problem of timing jitter between both lasers. An alternative method to achieve faster THz CT is the development of depth-resolving THz imaging with tomosynthesis which is similar to CT except that the number of projections is much smaller [12]. However, the efficiency of this system is mainly limited to thin samples. Furthermore, those methods are still based on point-by-point scanning measurements. If the pixel data could be measured in parallel simultaneously, the data acquisition time would be greatly reduced. 2D free-space electro-optics sampling (2D-FSEOS) enables us to acquire a 2D image of a sample in real-time [14]. Although 2D-FSEOS eliminates 2D scanning of the sample for THz CT, the mechanical time-delay scanning is still required. Finally, even if all those techniques can be used for THz-CT, they are still limited in practical use by the slow speed of final image acquisition.

Recently, we have developed a stage-free configuration combining single shot measurement of THz temporal waveform and one-dimensional (1D) transverse imaging, leading to real-time 2D spatio-temporal (2D-ST) THz imaging [15-17]. For this, we employed a combination of non-collinear electro-optic time-to-space conversion [18] with line focusing of a THz beam. Thanks to the elimination of both mechanical time-delay scanning due to time-to-space conversion and 1D sample scanning due to line focusing, THz reflective tomography [15] and spectral imaging of moving objects [16, 17] were successively demonstrated. Although this 2D-ST THz imaging is available for THz CT, the image acquisition time (typically a few tens to several tens seconds for one image) is still insufficient to achieve fast THz CT available for practical applications. Further decrease of the image acquisition time is indispensable to achieve fast THz CT.

Recent advance of intense THz source based on optical rectification in $LiNbO_3$ crystal associated with the tilted pulse front technique [19-24] revolutionizes THz imaging as well as THz nonlinear spectroscopy [25, 26]. For example, real-time 2D THz near-field imaging [27, 28] has been achieved by combining such an intense THz source with 2D near-field imaging technique based on 2D-FSEOS [29]. Furthermore, we recently demonstrated fast 2D THz spectral CT based on combination of this intense THz source with 2D-ST THz imaging and succeeded to measure cross-sectional images of continuously rotating samples in only a few seconds [30, 31]. If such fast THz CT can be extended to visualize 3D internal structure of the sample, the application field of THz-CT will be largely increased. In this article, we propose to demonstrate, for the first time to the best of our knowledge, the possibility of 3D THz CT by using an intense THz source and only two mechanical stages without reciprocating motion (one for continuous translation of sample and another one for incremental rotation of sample) instead of four, as pointed out previously. The system has been used to investigate test samples such as four metallic bars, a toothpick into a plastic case and a more realistic one consisting in a medicine capsule.

#182051 - $15.00 USD Received 19 Dec 2012; revised 17 Jan 2013; accepted 17 Jan 2013; published 24 Jan 2013

2. Experimental setup and 3D data processing

The 3D THz CT system is based on an amplified Ti:Sapphire laser with 1 kHz repetition rate, 0.8 mJ/pulse, 800 nm central wavelength and 150 fs pulse duration. The laser beam is splitted into pump and probe beams for THz generation and detection, respectively. The pump beam is sent onto an Au-coated 2000 mm/lines holographic grating to introduce the desired pulse front tilt and satisfy the phase matching condition for optical rectification in a stoichiometric $LiNbO_3$ crystal (1.5% Mg concentration), as shown in Fig. 1. Appropriate tilt angle and grating imaging into the crystal are controlled by two lenses (L1, f = 200 mm; L2, f = 100 mm). The pump beam is finally focused onto the crystal with a spot size of 2 × 2 mm^2. One surface of the crystal is cut with the phase matching angle of 62°. The generated THz beam is guided with an off-axis parabolic mirror (f = 190 mm), as shown in Fig. 1 where top and side views of the THz beam are presented for a better understanding of the line focusing and imaging optics. The THz beam is line-focused onto the sample using a THz cylindrical lens (THz-CL1, f = 50 mm, Tsurupica), resulting in a line of illumination (length = 25 mm, width = 1 mm) across the sample. Next, the line is imaged along the vertical Y-axis of a (110)-oriented ZnTe crystal (thickness = 1 mm, size = 25 × 25 mm^2) by a combination of a THz plano-convex lens (THz-L, f = 50 mm, Tsurupica) and a THz cylindrical lens (THz-CL2, f = 50 mm, Tsurupica). For detection, the probe beam is non-collinearly incident on the ZnTe crystal at a crossed angle of 25° with the THz beam. Since the temporal width of the probe pulse is much shorter than that of the THz pulse, wave fronts of the THz beam at different times overlap with that of the probe beam at different transverse positions. This non-collinear 2D-FSEOS provides a time-to-space conversion of the pulsed THz electric field, such as a single-shot autocorrelator [18]. After passing through two crossed polarizers (P and A), the spatial intensity distribution of the probe beam induced by the spatial birefringence distribution in the EO crystal is imaged with a plano-convex lens (L3, f = 80 mm) onto a high-speed CMOS camera (232 × 232 pixels, 1000 frames per second) synchronized with the 1 kHz laser pulse.

The resulting image, called “2D-ST image”, is composed of the time profile of the THz pulse (temporal window = 37 ps) and the line image (spatial range = 25 mm) of the sample, which are developing along horizontal and vertical coordinates of the camera, respectively. This THz image was acquired at a frame rate of 500 Hz by the CMOS camera working in the dynamic subtraction mode [32]. Finally, owing to the 10 ms integration time of the CMOS camera, the 2D-ST image is acquired with a 100 Hz acquisition rate. The transverse resolution along the line projection attains the diffraction limit of the imaging system [16]. The pixel number in the vertical direction of the 2D-ST image is 232 pixels, which provides a pixel rate of 2320 pixels/s. This is much faster than conventional THz imaging system where pixel rate is usually from 1 to 100 pixels/s. However, as for 3D CT it is important to limit the amount of data storage, we arbitrarily reduced the size of the 2D-ST image to 116 × 116 pixels. Data storage and total acquisition time of our 3D THz CT system will be presented into more details in Table 1.

#182051 - $15.00 USD Received 19 Dec 2012; revised 17 Jan 2013; accepted 17 Jan 2013; published 24 Jan 2013

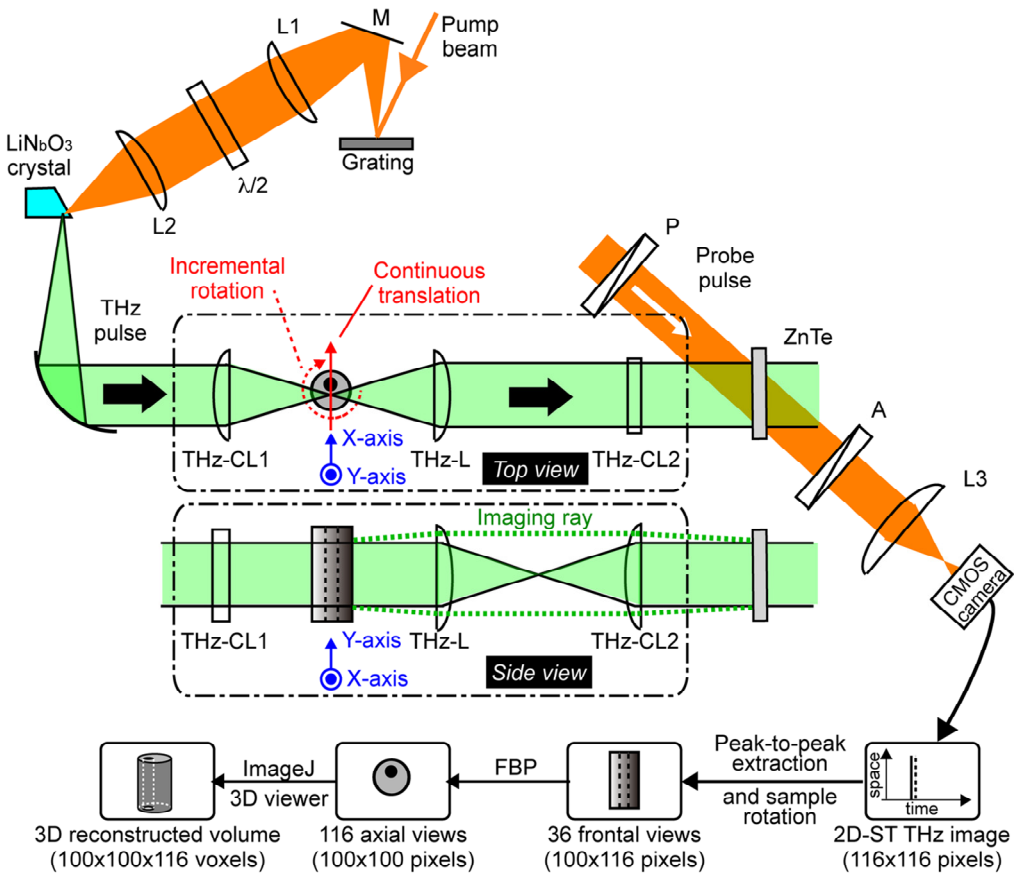

Fig. 1. Experimental setup and schematic representation of final 3D reconstruction (in the case of 36 projections). THz-CL1 and THz-CL2: Tsurupica THz cylindrical lenses, THz-L: Tsurupica THz plano-convex lens, P: polarizer, A: analyzer, L: plano-convex lens.

To perform fast 3D THz CT, the sample is horizontally scanned along the X-axis with a translation stage at a constant speed of 2 mm/s whereas the THz beam is vertically line-focused along Y-axis of the sample so that a series of 2D-ST images can be acquired for a given projection angle. Unfortunately, the acquisition time to get the series of 2D-ST images is limited by the maximum scan speed (= 2 mm/s) of the translation stage although the integration time of a 2D-ST image is only 10 ms. For instance, for a 20 mm scan range (acquisition time of 10 s), we usually record 100 2D-ST images corresponding to 100 horizontal pixels. We believe that it should be possible to further reduced the acquisition time down to only 1 s if a translation stage with 10-times faster scan speed (20 mm/s) can be used. Next, the sample is rotated (angle step of 5°) and a second 2D-ST image set is recorded. The operation is repeated 36 times from 0° to 175°. Finally, the total acquisition time corresponding to 36 projections is only 6 minutes. This shows a significant reduction in the measurement time compared with standard 3D THz CT systems using point-to-point scanning measurement (typically from 1 to 10 hours).

Finally, for each projection angle and at every horizontal and vertical sample positions, the pixel value is extracted by measuring the peak-to-peak value of the THz electric field in temporal waveform. Similarly, after FFT of temporal data, the spectral amplitude at a given frequency could also be extracted for spectral imaging [30]. Then, the application of the well-known FBP algorithm implemented in the ImageJ software will numerically provide the multiplanar slices of the sample in order to finally reconstruct the 3D volume [33]. It is well-known that FBP suffers from several drawbacks such as beam hardening, which can induce

#182051 - $15.00 USD Received 19 Dec 2012; revised 17 Jan 2013; accepted 17 Jan 2013; published 24 Jan 2013

cupping, streaks and blurring because rays from some projection angles are hardened to a differing extent than rays from other angles, confusing the reconstruction algorithm. To reduce this phenomenon, it is important to record at least 36 projections. Of course, depending on maximum data storage and acquisition time fixed by the operator, it is also possible to record 72 projections with a 2.5° angle step. However, we considered that the best compromise between reconstruction quality (contrast, intensity and geometric preservation) and acquisition time consists in recording only 36 projections [34]. To summarize the experimental conditions and data processing, Table 1 provides the total acquisition time and laptop data processing of the 3D THz CT for 36 projections, 20 mm horizontal scan with 100 pixels (continuous speed of 2 mm/s) recording and 116 vertical pixels. Main remarkable feature is the short total acquisition time of only 6 minutes for this experiment associated with reasonable data storage of 295 MB.

Table 1. Acquisition time and laptop data processing of the fast 3D THz CT

	Data acquisition			**Data processing**	
	2D-ST image 116 × 116 pixels	Sample translation 2 mm/s 100 pixels	Sample rotation to get 36 projections	Peak-to-peak analysis of 2D-ST images to get the 36 frontal views	FBP algorithm to get the 116 axial views
Time (s)	0.01	10	360	240	60
Data storage (MB)	0.082	8.2	295	1.58	4.35

3. Experimental results and discussion

3.1 Comparison between optical rectification in $LiNbO_3$ and ZnTe crystals for 2D-ST THz imaging

In this sub-section, we want to evaluate the basic performances (i.e. maximum THz electric field and dynamic range) of 2D-ST THz imaging using optical rectification in $LiNbO_3$ crystal as compared to ZnTe crystals.

First, we estimated the maximum THz electric field in the 2D-ST THz image. Unfortunately, since this 2D-ST THz image was obtained by FSEOS near the zero optical transmission point (crossed Nichol configuration for the probe beam, Fig. 1), it is difficult to calibrate the absolute value of the THz electric field directly from the measurement of the induced phase modulation [20, 23]. Alternatively, we modified the optical setup for THz detection in Fig. 1 to collinear FSEOS detection composed by a (110)-oriented GaP crystal (thickness = 0.3 mm) and two balanced photodiodes (not shown in Fig. 1) while maintaining the same setup for generation of intense THz pulse. Figure 2 shows the temporal evolution of the corresponding electric field E_{THz} evaluated from the EO signal, in which the electric field amplitude in the left axis has been calibrated according to the procedure of previous papers [20, 23]. The maximum amplitude of the THz electric field achieves 170 kV/cm, which is more than one order of magnitude higher than standard THz source using optical rectification in ZnTe (typically, a few tens kV/cm).

In the above experiment, the intense THz beam was point-focused onto the GaP crystal with a spot diameter of about 1 mm, resulting in the maximum electric field of 170 kV/cm. On the other hand, in the 2D-ST THz imaging, this intense THz beam is sent onto the ZnTe crystal with a beam diameter of about 25 mm. Taking into account this expansion factor of 25 for the THz beam, we can roughly estimate that the maximum electric field of the intense THz beam at the ZnTe crystal position in the case of 2D-ST THz imaging is about 7 kV/cm. For that, we simply argue that the electric field is inversely proportional to the beam radius for a given energy of the THz beam [35]. Of course, for further practical applications, it would be useful to get a THz line illumination of 50 mm onto the sample. If we want to keep the same dynamic range for the THz detection, we can estimate that this would require a THz electric field of 340 kV/cm, which may be achievable with an increase of the incident laser

#182051 - $15.00 USD Received 19 Dec 2012; revised 17 Jan 2013; accepted 17 Jan 2013; published 24 Jan 2013

pulse energy onto the $LiNbO_3$ crystal. Figure 3(a) shows a 2D-ST THz image in the absence of a sample after integrating 5 images (corresponding measurement time = 10 ms). The green and red areas in the image indicate positive and negative electric field, respectively. The main THz pulse is visible around 6 ps (additional THz pulse around 28 ps is a replica generated by the ZnTe crystal). Figure 3(b) shows a temporal waveform of the THz electric field extracted along the dashed white line in the 2D-ST THz image. The color scale in Fig. 3(a) and vertical axis in Fig. 3(b) have been calibrated based on the expansion factor of the THz beam, as explained previously. Here, it is worth to emphasize that this intense THz source maintains a maximum electric field similar to that of a point-focused THz beam from usual ZnTe-based THz source. This is due to the large enhancement of THz electric field even though the THz beam is not focused onto the crystal in our experimental setup. It is worth noting that, according to Kristensen *et al.* [36], such an intense THz pulsed electric field will give a negligible temperature increase of a water content sample. These authors mentioned that if the THz beam is focused down to a spot size of 0.5 mm, the steady-state temperature increase per mW of transmitted power is 1.8 °C/mW. In our case, the maximum THz beam power sent onto the sample is in the order of a few tens of to one hundred microwatts associated to a line focusing of 1×25 mm^2. This indicates that heating effects on water can be neglected in our measurements which can be essential for further biological applications.

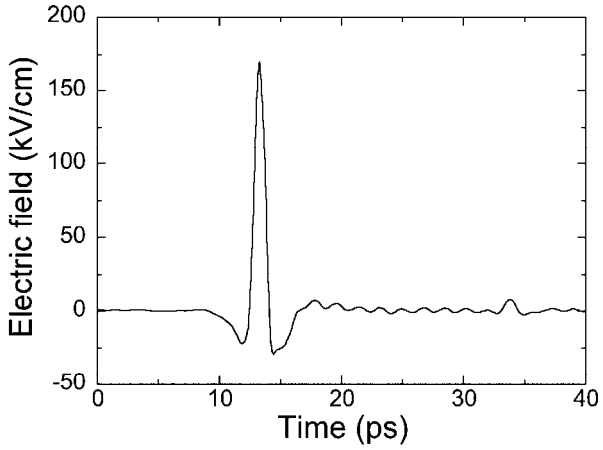

Fig. 2. Temporal profile of THz electric field generated by optical rectification from $LiNbO_3$. Collinear FSEOS detection with a (110)-oriented GaP crystal (thickness = 0.3 mm) and balanced photodiodes are used for this measurement.

#182051 - $15.00 USD Received 19 Dec 2012; revised 17 Jan 2013; accepted 17 Jan 2013; published 24 Jan 2013

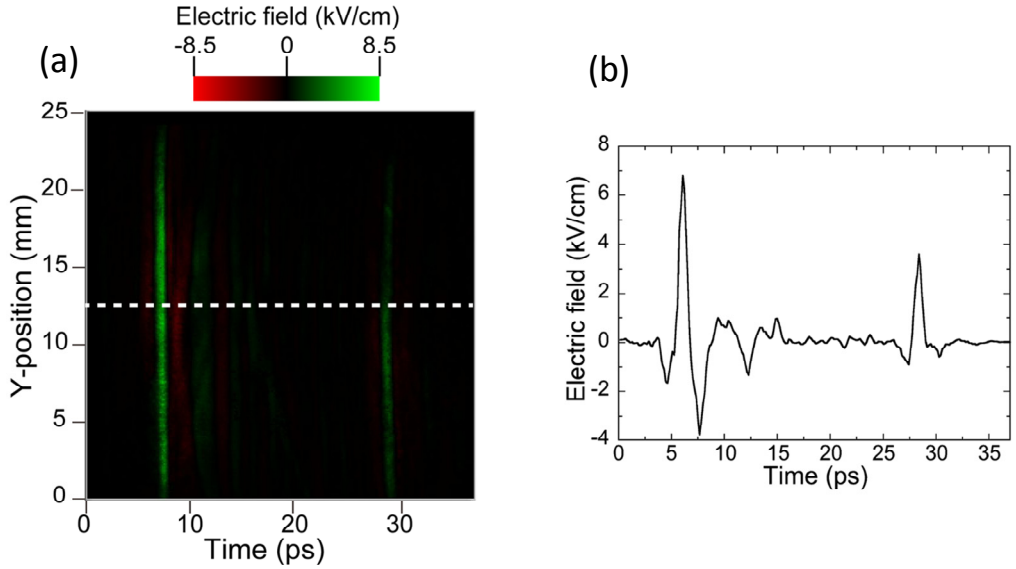

Fig. 3. (a) 2D-ST THz image and (b) temporal waveform of the pulsed THz electric field along white line in panel (a). Non-collinear FSEOS detection with a (110)-oriented ZnTe crystal (thickness = 1 mm) and CMOS camera were used for this measurement.

Next, we investigated the dynamic range in the temporal waveform of THz electric field extracted from a 2D-ST image. Here, the dynamic range is defined as a ratio of a peak-to-peak value of pulsed electric field in the presence of THz beam to a standard deviation of noise signal in the absence of THz beam. Figure 4 shows the result for the present THz-CT system based on optical rectification in $LiNbO_3$ crystal. For comparison, we also plotted the similar dynamic range obtained with our previous system using optical rectification in ZnTe crystal [16, 17]. One can confirm that the dynamic range is largely enhanced in $LiNbO_3$ crystal combined with tilted pulse front technique compared to collinear phase-matching in ZnTe crystal. For example, at an integration time of 10 ms (100 Hz frame rate), the dynamic range is 619 with $LiNbO_3$ and only 49 with ZnTe. This confirms the potential of optical rectification in $LiNbO_3$ crystal using tilted pulse front for fast THz imaging applications, as shown in the next sub-sections.

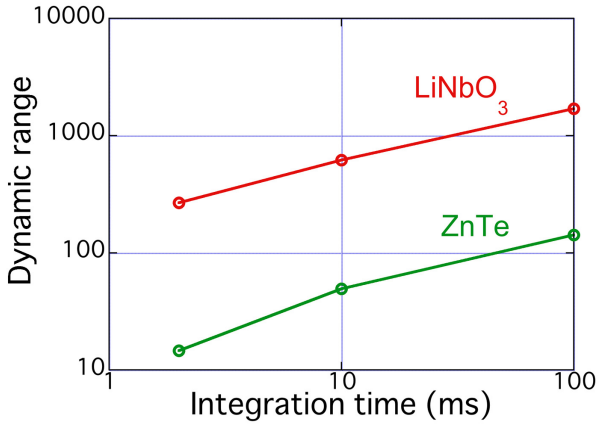

Fig. 4. Dynamic range of the temporal waveform extracted from 2D-ST THz image as a function of the integration time in the case of optical rectification in $LiNbO_3$ (tilted pulse front) and ZnTe (collinear phase-matching).

#182051 - $15.00 USD Received 19 Dec 2012; revised 17 Jan 2013; accepted 17 Jan 2013; published 24 Jan 2013

3.2 Fast 3D THz CT

To demonstrate the ability of fast 3D THz CT, we first investigated a simple test sample consisting of four vertical asymmetric metallic bars (2 mm diameter), as shown in an inset of Fig. 5(a), illuminated by the vertical THz focal line. As explained previously, 3D CT is performed in only 6 minutes after continuous horizontal translation (2 mm/s, 100 pixels) of the sample and 36 rotations with a 5° angle step in order to collect the projection data. From these raw data, after the peak-to-peak extraction of the THz electric field, we can visualize the frontal views (XY-plane) of the sample corresponding to the different projections. One of these views (100 × 116 pixels) is presented in Fig. 5(a), showing the position of the four asymmetric bars, white and black colors indicating weak and strong transmitted THz signal, respectively. From this image, we can clearly see the arrangement of the sample consisting in two long bars at the extremities and two shorter ones in the middle. Diffraction effects can also be observed near the edges of the two central bars. The video (36 projections) is available in Media 1 and makes it possible to clearly see the position of the bars from each other. Using the standard FBP algorithm [1], we can reconstruct the 116 cross-sectional images (also called "axial view") corresponding to the portion of the object illuminated by the THz line. Figure 5(b1) shows the axial view corresponding to the position of the upper red horizontal line in Fig. 5(a), whereas Fig. 5(b2) is for the lower red horizontal line. From these two cross sections, it is obvious to identify the respective position of all the bars from each other, with a good contrast (no THz signal through the metallic bars) and a sub-millimeter spatial resolution. Finally, using the ImageJ software, the 3D reconstruction of the sample can be obtained, as shown in Fig. 5(c) which corresponds to one still picture from the 3D movie (available in Media 2). We have to notice that inhomogeneities in thickness over the complete length of the bars can be visible in Figs. 5(a) and 5(c), attributed to peak-to-peak extraction errors and reconstruction artifacts inherent to the FBP algorithm.

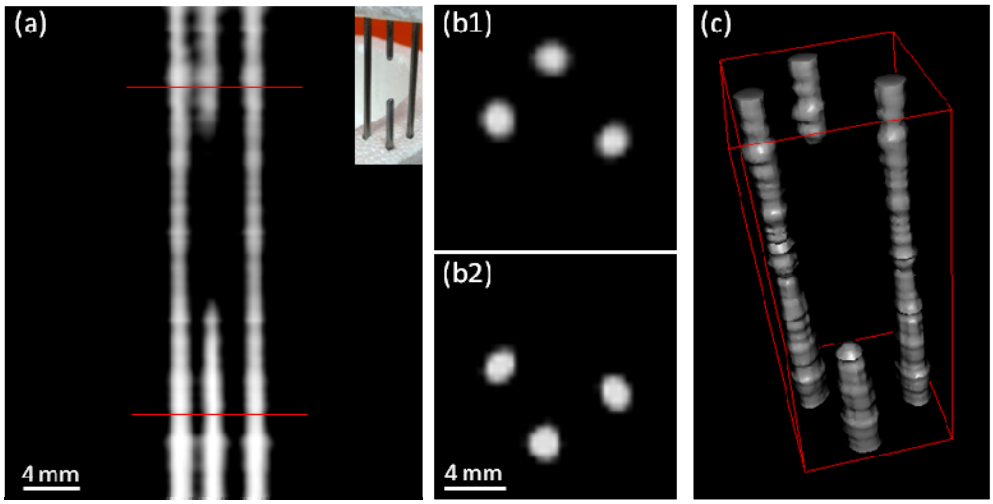

Fig. 5. Four metallic bars. (a) Frontal view (Media 1) and picture of the sample (inset). (b1) Axial view from the upper red line in (a). (b2) Axial view from the lower red line in (a). (c) 3D reconstruction (Media 2).

The second test sample is a plastic box (section 10 × 10 mm^2) with a wooden toothpick inside. Similarly, Fig. 6(a) shows one of the 36 frontal views (video in Media 3), Figs. 6(b1) and 6(b2) give the two axial views at the position of the red horizontal lines, and Fig. 6(c) is the final 3D reconstruction including a picture of the sample as inset (video in Media 4). First, we can notice that we are able to determine the position of the toothpick inside the plastic box in all figures. Then, especially from the axial views, we observe that the shape of the rectangular plastic box is not perfectly reconstructed. This comes for the relative transparency

#182051 - $15.00 USD Received 19 Dec 2012; revised 17 Jan 2013; accepted 17 Jan 2013; published 24 Jan 2013

of the plastic material for THz radiation giving a weak attenuation of the transmitted THz pulse except around the four corners, which are much clearly visible in the figure. These first two examples demonstrate the ability of the system to properly reconstruct in a relatively short time the 3D shape of simple samples.

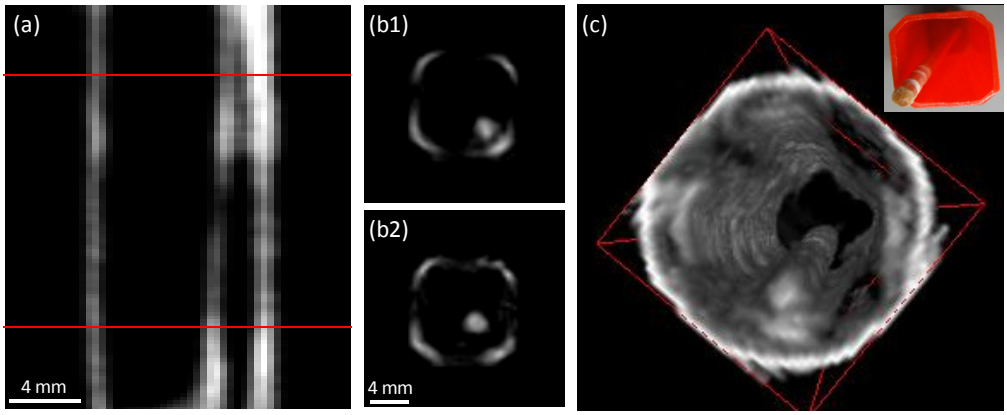

Fig. 6. A wooden toothpick into a plastic case. (a) Frontal view (Media 3). (b1) Axial view from the upper red line in (a). (b2) Axial view from the lower red line in (a). (c) 3D reconstruction (Media 4). Inset: picture of the sample.

The last object is a gelatin soluble capsule enclosing a dose of medicine powder (inset in Fig. 7(a), object size: 7 × 20 mm). This sample represents a more realistic object in order to test the potential of the system for pharmaceutical applications. From the frontal view [Fig. 7(a)], it is possible to clearly see the capsule with the localization of its internal content. We note that the extreme lower part of the capsule is not imaged because it is attached on a metallic rod for precise rotation. Of course, from the peak-to-peak analysis, it is not possible to get any information from the chemical structure of the medicine powder. This should require a spectroscopic analysis of the 2D-ST image as in ref 29. Here, we can observe that THz radiation is totally absorbed by the medicine powder. Consequently, it is impossible to get any information on the powder homogeneity from this measurement. From this view, it is also not possible to see the separation between the two semi-cylindrical gelatin parts constituting the capsule because the amount of medicine powder is too high. However, the axial views make it possible to see the empty part of the capsule (Fig. 7(b1)) and the localization of the powder [Fig. 7(b2)]. Finally, Fig. 7(c) and Media 5 show the 3D reconstruction of the capsule which is useful to get a global view of the object even if, for a quantitative visualization of 3D objects using CT, mainly axial and front views are used. From this 3D view, even if the powder is clearly identified in the lower part of the capsule, its outer shape is not perfectly reconstructed. Especially, the top of the capsule presents some reconstruction artifacts, probably due to diffraction effects and THz beam deviation occasioned by the spherical shape of the sample in this region.

#182051 - $15.00 USD Received 19 Dec 2012; revised 17 Jan 2013; accepted 17 Jan 2013; published 24 Jan 2013

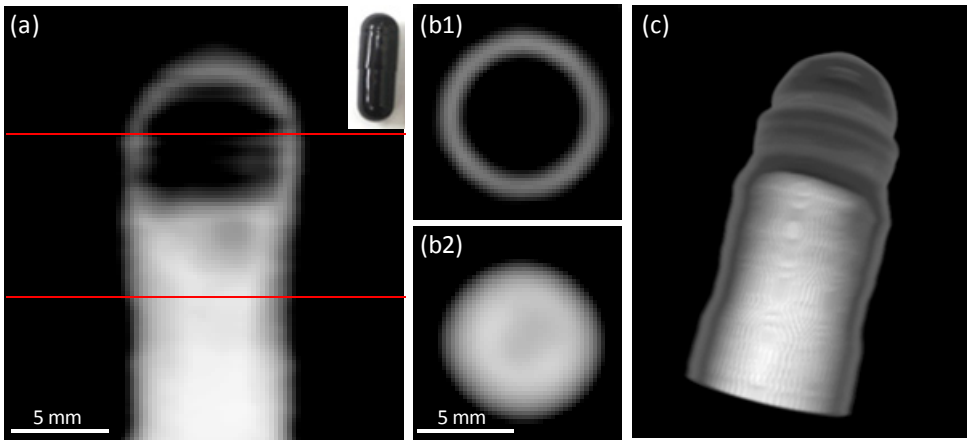

Fig. 7. Medicine capsule. (a) Frontal view (inset: photograph). (b1) Axial view from the upper red line in (b). (b2) Axial view from the lower red line in (b). (c) 3D reconstruction (Media 5).

4. Conclusion

In this paper, we demonstrated the potential of intense THz pulse generated by optical rectification in $LiNbO_3$ crystal for 3D THz CT. We estimated that the maximum amplitude of the electric field of the 25 mm diameter THz beam attained 7 kV/cm. We also measured a dynamic range of 619 for the THz detection at the integration time of 10 ms, which is 13-times higher than that of our previous system based on collinear optical rectification in ZnTe crystal [16, 17]. The main advantage of the proposed method relies on real-time THz line projection providing 10 ms acquisition time of 2D-ST THz image. Therefore, 3D THz CT has been performed in only 6 minutes, representing a significant improvement compared with common systems. The use of another translation stage with 10-times faster speed will further decrease the total measurement time for 3D THz CT down to only 36 s. Finally, demonstration of 3D reconstructions of selected samples clearly indicated a high potential for sensing, non-destructive inspection and material characterization in real world applications.

Acknowledgments

E. Abraham is grateful to the BRIDGE Fellowship Program, Japan Society for the Promotion of Science, Japan. This work was supported by Grants-in-Aid for Scientific Research 21650111 and 23656265 from the Ministry of Education, Culture, Sports, Science, and Technology of Japan. We also gratefully acknowledge financial support from the Renovation Center of Instruments for Science Education and Technology at Osaka University, Japan.

#182051 - $15.00 USD Received 19 Dec 2012; revised 17 Jan 2013; accepted 17 Jan 2013; published 24 Jan 2013